



Ceria nanoparticles shape effects on the structural defects and surface chemistry: Implications in CO oxidation by Cu/CeO₂ catalysts

Maria Lykaki^a, Eleni Pachatouridou^b, Sónia A.C. Carabineiro^c, Eleni Iliopoulou^b,
Chrysanthi Andriopoulou^d, N. Kallithrakas-Kontos^e, Soghomon Boghosian^d,
Michalis Konsolakis^{a,*,1}

^a School of Production Engineering and Management, Technical University of Crete, GR-73100, Chania, Crete, Greece

^b Chemical Process & Energy Resources Institute (CPERI), Centre for Research & Technology Hellas (CERTH), 6th km. Charilaou—Thermi Rd., P.O. Box 60361, GR-57001, Thermi, Thessaloniki, Greece

^c Laboratório de Catálise e Materiais (LCM), Laboratório Associado LSRE-LCM, Faculdade de Engenharia, Universidade do Porto, 4200-465, Porto, Portugal

^d Department of Chemical Engineering, University of Patras and FORTH/ICE-HT, GR-26504, Patras, Greece

^e School of Mineral Resources Engineering, Technical University of Crete, GR-73100, Chania, Crete, Greece

ARTICLE INFO

Keywords:

Ceria nanoparticles
Shape effects
Cu/CeO₂ mixed oxides
In situ Raman
CO oxidation

ABSTRACT

Copper-ceria binary oxides have been extensively used in a wide variety of catalytic processes due to their unique catalytic features in conjunction to their lower cost as compared to noble metal-based systems. However, various parameters related to different counterparts characteristics, such as particle size and morphology, can exert a profound influence on the structural/redox properties of binary oxides and, consequently, on their catalytic performance. Here, we report on ceria nanoparticles shape effects: nanorods (NR), nanopolyhedra (NP) and nanocubes (NC) on the solid state properties of copper-ceria binary oxides. A thorough characterization study by both *ex situ* (surface area determination, X-ray diffraction, X-ray fluorescence, H₂-temperature programmed reduction, transmission electron microscopy, X-ray photoelectron spectroscopy) and *in situ* (Raman spectroscopy) techniques was undertaken to gain insight into the impact of the support morphology on the surface, structural and redox properties. A novel approach based on sequential *in situ* Raman spectra obtained under alternating oxidizing and reducing atmospheres was employed to reveal the impact of ceria exposed facets on the structural defects. CO oxidation was employed as a probe reaction to disclose structure-property relationships. The results clearly revealed the key role of ceria morphology rather than structural/textural characteristics on the reducibility and oxygen mobility, following the sequence: NR > NP > NC. The latter seems to have a profound influence on copper-ceria interactions towards the stabilization of Cu⁺ species, via Ce⁴⁺/Ce³⁺ and Cu²⁺/Cu⁺ redox equilibrium. Interestingly, CuO incorporation in different ceria carriers boosts the catalytic activity without, however, affecting the order observed for bare ceria, i.e., CeO₂-NR > CeO₂-NP > CeO₂-NC, implying the key role of support. The Cu/CeO₂ sample with the rod-like morphology exhibited the highest catalytic performance, offering almost complete CO elimination at temperatures as low as 100 °C. A perfect relationship between the catalytic performance and the following parameters was disclosed, on the basis of a Mars-van Krevelen mechanism: i) abundance of weakly bound oxygen species, ii) relative population of Cu⁺/Ce³⁺ redox pairs, iii) relative abundance of defects and oxygen vacancies.

1. Introduction

Cerium oxide or ceria (CeO₂) has gained considerable attention in numerous catalytic processes, such as toxic emissions abatement, diesel soot removal, wastewater treatment, water-gas shift, steam reforming, etc. [1]. This is mainly due to the enhanced thermal stability of ceria in

conjunction to its high oxygen storage capacity (OSC) and oxygen mobility [2–4]. In fact, the facile transition between the Ce³⁺ and Ce⁴⁺ oxidation states, linked to the formation and annihilation of surface/structural defects (i.e. oxygen vacancies), is considered responsible for the superior redox properties of ceria [3,5–7].

Although the majority of ceria-based applications relies on ceria

* Corresponding author.

E-mail address: mkonsol@science.tuc.gr (M. Konsolakis).

¹ URL: <http://www.tuc.gr/konsolakis.html>.

particles of not well defined morphology, recent theoretical [2,8,9] and experimental [10–17] studies have revealed that the redox and, in consequence, the catalytic properties of ceria can be significantly enhanced by tailoring the shape and size of the particles. In fact, ceria functionalization *via* nanosynthesis routes can exert significant alterations on the structural, surface and redox properties, arising from quantum size effects [14,18].

Nano-ceria exhibits abundance of defect sites (e.g. oxygen vacancies) and surface atoms, when compared to the bulk counterpart. Numerous studies [11,19–23] have focused on the fine-tuning of ceria through the development of materials with predefined structural and textural characteristics. On the other hand, it was clearly revealed that the energy formation of anionic vacancies is dependent on the exposed nanocrystals facets, following the sequence: $\{111\} > \{100\} > \{110\}$. In this regard, research efforts have been devoted to the synthesis of ceria nanoparticles with abundance of active crystal planes [14,20,22–27]. In view of this fact, we recently showed that ceria nanorods, exposing $\{100\}$ and $\{110\}$ crystal planes, exhibited the optimum CO oxidation activity, among ceria samples of different morphology. By means of complementary characterization studies, a direct relationship between the abundance of loosely bound oxygen species and catalytic activity was established [28].

Despite the excellent redox properties of bare ceria that can be further adjusted by engineering its shape and size, the majority of heterogeneous catalysts are based on supported systems rather than on individual counterparts, in view of the fact that “the whole is more than the sum of its parts” [19,29]. Combining ceria with transition metals can improve the catalytic performance due to a peculiar synergistic effect linked to metal-support interactions [19,30,31]. Electronic, geometric and bifunctional interactions between both components are thought to be responsible for the enhanced performance of mixed oxides, when compared to bare oxides [32]. Despite the progress in the field, the fundamental understanding and the experimental verification of the aforementioned “synergistic” phenomena are still under debate [19,29].

Among the different ceria-based catalysts, the copper-ceria system has triggered a substantial interest in heterogeneous catalysis, due to its unique catalytic properties and lower cost compared to noble metal-based catalysts. Nowadays, it is well documented that the complex copper-ceria interactions can account for the enhanced catalytic performance. The advances in relation to the role of copper-ceria interactions in catalysis have been recently comprehensively reviewed [33]. Based on the most constructive experimental and conceptual studies, the superiority of Cu/CeO₂ system can be mainly ascribed to a synergistic effect. In particular, various interrelated phenomena were revealed to affect the interfacial interactions with great consequences on the catalytic performance: (i) electronic perturbations between copper and ceria nanoparticles, (ii) facilitation of the interplay between Cu²⁺/Cu⁺ and Ce³⁺/Ce⁴⁺ redox couples, (iii) facilitation of oxygen vacancies formation, (iv) enhanced oxygen mobility and reducibility, (v) formation of interfacial sites of unique activity [33].

In light of the above aspects, the adjustment of ceria oxide characteristics, in terms of size and morphology, can exert a profound influence on the aforementioned parameters with great implications in catalysis [17,33–37]. For instance, Ouyang et al. [26] found that Cu supported on ceria nanorods exhibited the optimum CO₂ hydrogenation activity among different ceria morphologies (nanorods, nanocubes, nanoparticles), ascribed to the strong interaction between copper and ceria nanorods. On the other hand, copper-ceria nanospheres/octahedrons exhibited the optimum water-gas shift activity in comparison with nanorods and nanocubes, which was attributed to the presence of defects and imperfections in the support that favoured strong metal-support interactions, as generally stated [27,36]. In a similar manner, the exposed facets of $\{111\}/\{100\}$ of copper-ceria nanospheres exhibited higher activity than nanorods for CO oxidation, due to the existence of more reducible CuO_x clusters on the nanospheres' surface

[38]. In general, the different exposed crystal planes of ceria can alter the geometry and coordination environment of copper ions, affecting the catalytic activity of Cu/Ceria binary system in different ways, depending on reaction environment [14,25,36,38–40].

Despite the intense interest in the field, the fundamental origin of nanoceria shape effects in catalysis is still a matter of debate. In particular, there is still a lack of atomistic understanding concerning the impact of exposed facets on the solid state properties and, in turn, on the catalytic performance of ceria-based catalysts. In the present work, three different ceria nanostructures (rods, polyhedra, cubes) were prepared by the hydrothermal method and employed as supporting carriers for Cu-based catalysts. Various *ex situ* (surface area determination, X-ray diffraction, X-ray fluorescence, H₂-temperature programmed reduction, transmission electron microscopy, X-ray photoelectron spectroscopy) and *in situ* (Raman spectroscopy) characterization techniques were employed to gain insight into the impact of ceria exposed facets on the structural defects and surface chemistry of copper-ceria binary oxides. CO oxidation was employed as probe reaction to reveal the structure-activity relationships.

2. Experimental

2.1. Materials synthesis

All chemicals used in this work were of analytical reagent grade. Ce(NO₃)₃·6H₂O (purity ≥ 99.0%, Fluka) and Cu(NO₃)₂·2.5H₂O (Fluka) were used as precursors for the preparation of ceria and Cu/Ceria materials. NaOH (purity ≥ 98%, Sigma-Aldrich) and ethanol (purity 99.8%, ACROS) were also employed during the synthesis procedure. Bare ceria nanoparticles were initially synthesized by the hydrothermal method [28]. For the synthesis of ceria nanorods (CeO₂-NR), 2.75 mol NaOH was initially dissolved in 75 mL of double deionized water. Then, 175 mL of aqueous solution containing 23 mmol Ce(NO₃)₃·6H₂O (0.13 M) was added in the above solution under vigorous stirring until the formation of a milky slurry. The mixture was left for additional stirring for 1 h. The final slurry was then transferred into a Teflon bottle and aged at 90 °C for 24 h. To obtain the CeO₂-NP sample, the same procedure was followed as above with only one variation: 0.45 mol NaOH instead of 2.75 mol was utilized. For the synthesis of ceria nanocubes (CeO₂-NC), the procedure followed for the preparation of Ceria-NR was employed, whereas the final aging was performed at 180 °C instead of 90 °C. Afterwards, the solid products were recovered by centrifugation. The materials were washed thoroughly with double deionized water until pH 7, in order to remove any co-precipitated salts and then washed with ethanol to avoid agglomeration. The precipitate was dried at 90 °C for 12 h, followed by calcination at 500 °C for 2 h under air flow (heating ramp 5 °C/min).

Cu/CeO₂-NX (NX: NP – nanopolyhedra, NR – nanorods, NC – nanocubes) catalysts were synthesized by the wet impregnation method, using an aqueous solution of Cu(NO₃)₂·2.5H₂O so as to obtain a Cu/(Cu + Ce) atomic ratio of 0.2, corresponding to a Cu loading of 8.5 wt. %. The resulting suspensions were heated under stirring until water evaporation, dried at 90 °C for 12 h and finally calcined at 500 °C for 2 h under air flow (heating ramp 5 °C/min). This specific pre-treatment is selected in order to establish a stable catalyst state, not sensitive to reaction environment (maximum temperature of 500 °C; 2000 ppm CO and 1.0 vol.% O₂ in He).

2.2. Materials characterization

The textural characteristics of the as-prepared catalysts were determined by N₂ adsorption-desorption isotherms obtained at –196 °C (Nova 2200e Quantachrome flow apparatus). Specific surface areas (m²/g) were obtained according to the Brunauer-Emmett-Teller (BET) method at relative pressures in the 0.05–0.30 range. The specific pore volume (cm³/g) was calculated based on the highest relative pressure,

whereas the average pore size diameter (d_p , nm) was determined by the Barrett-Joyner-Halenda (BJH) method. Prior to measurements the samples were degassed at 250 °C for 5 h under vacuum.

The crystalline structure of ceria sample was determined by powder X-ray diffraction (XRD) on a Siemens D 500 diffractometer operated at 40 kV and 30 mA with Cu K α radiation ($\lambda = 0.154$ nm). Diffractograms were recorded in the 2–80° 2 θ range and at a scanning rate of 0.02° s^{−1}. The Scherrer Eq. (1) was employed to determine the primary particle size of a given crystal phase based on the most intense diffraction peak of CeO₂ (2 θ : 28.5° and 47.6°) and CuO (2 θ : ~35.3° and 38.2°) patterns:

$$D_{\text{XRD}} = \frac{K\lambda}{\beta \cos \theta} \quad (1)$$

where K is the Scherrer constant; λ is the wavelength of the X-ray in nm; β is the line broadening; θ is the Bragg angle [41].

X-ray Fluorescence (XRF) analyses were performed on an X-ray spectrometer (Amptek X-123) with Si-PIN photodiode. The X-ray spectrometer contains a solid-state detector, a digital pulse processor and a multichannel analyzer, which are interfaced with a computer for data acquisition and analysis. A 25 μ m thick silver filter and a 250 μ m thick aluminum filter were simultaneously used to reduce background and improve signal-to-noise ratio (SNR) in the energy region (10–30 keV) of the XRF spectrum. The distance between the X-ray tube and the sample as well as between the detector and the sample were 1 cm. A series of Cu/Ceria reference samples with a Cu loading in the range of 1–15 wt.% were employed to obtain a calibration curve. Analysis was performed by the AXIL(RN) software package supplied by the International Atomic Energy Agency [42].

Temperature Programmed Reduction (H₂-TPR) experiments were carried out in a fully automated AMI-200 Catalyst Characterization Instrument (riments were carried out in a fully automated AMI-200 Catalyst Characterization Instrument (Altamira Instruments) under H₂ atmosphere, to acquire information on the reducibility of the samples. In a typical TPR experiment, ~50 mg of sample was placed in a U-shaped quartz tube, located inside an electrical furnace, and heated up to 1100 °C at 10 °C/min under He flow of 29 cm³/min and H₂ flow of 1.5 cm³/min. The H₂ consumption was calculated by the integrated area of TPR peaks, calibrated against a known amount of CuO standard sample [43,44].

XPS analysis was performed using a Kratos AXIS Ultra HSA, with VISION software for data acquisition and CASAXPS software for data analysis. The samples were pressed into pellets with ~1 mm thickness and attached to the sample holder with a small cut of double side carbon tape. The analysis was performed with a monochromatic Al K α X-ray source (1486.7 eV), operating at 15 kV (90 W), in FAT mode (Fixed Analyser Transmission), with a pass energy of 40 eV for regions (ROI) and 80 eV for survey. Data acquisition was performed with a pressure lower than 1 \times 10^{−6} Pa, employing a charge neutralisation system. The effect of the electric charge was corrected by the reference of the carbon peak C 1s (285 eV). The fitting of peak spectra was performed using the CasaXPS software, using Gaussian-Lorentzian peak shape and Shirley (or Linear) type background subtraction.

Transmission electron microscopy (TEM) analyses were performed on a Leo 906 E apparatus, at 100 kV. Samples were prepared by ultrasonic dispersion in ethanol and placed on a copper grid for analysis.

In situ Raman spectroscopic measurements were undertaken by using a homemade optical Raman cell, described in detail elsewhere [45]. Approximately 150 mg of powdery sample were pressed into a wafer disc that was mounted on the sample holder of the *in situ* cell by means of a gold wire. Temperature was controlled and monitored with a thermocouple located very close to the sample. The 491.5 nm line of a Cobolt Calypso diode-pumped solid state laser operated at a power level of less than 20 mW (on the sample) was used for exciting the Raman spectra. The incident laser beam was slightly defocused by means of a cylindrical lens in order to exclude excessive sample irradiance. The sampling depth of the 491.5 nm laser is several hundred molecular

layers, which combined with the area of the irradiation spot result in a considerable sampling volume that is characteristic of the bulk. Changing the irradiation spot did not cause changes in the *in situ* Raman spectra. The scattered light was collected at right angle (horizontal scattering plane) and analyzed with a 0.85 m Spex 1403 double monochromator with PMT (−20 °C cooled RCA) detection interfaced with a Labspec acquisition software.

For recording the *in situ* Raman spectra a recently described protocol was followed [46]. Briefly, each sample was first heated in the *in situ* Raman furnace under flowing 20%O₂/He (30 cm³/min) at a temperature of 440 °C and subjected to the flowing gas for 30 min and the *in situ* Raman spectrum was recorded under oxidizing conditions at 440 °C. Subsequently, the flowing feed gas was switched to 5%H₂/He (50 cm³/min) at the same temperature (440 °C) and the sample was subjected to flowing reducing atmosphere for 1 h and 45 min in order to attain steady state and the *in situ* Raman spectrum was recorded at 440 °C. A subsequent reoxidation of the sample was performed to check that the initial features of the Raman spectra obtained under oxidizing conditions could be reinstated. The temperature of 440 °C was chosen, after undertaking the H₂-TPR measurements, in order to achieve an observable spectroscopic effect [46] upon subjecting each sample in oxidation/reduction cycles.

As before [46], for comparison purposes, normalized and so-called “reduced” Raman spectra are used. The normalization procedure eliminates the effect of variations in absorption of incident and scattered light by differently colored samples, whereas in order to disentangle the effects caused by temperature (depopulation of ground state, etc.) and focus on the purely vibrational effects the “reduction” procedure is applied [46]. Briefly, the Stokes reduced intensity is given by:

$$I_R(\tilde{\nu}) = \frac{\tilde{\nu}}{(\tilde{\nu}_0 - \tilde{\nu})^4} \left[\frac{1}{\exp(hc\tilde{\nu}/k_B T) - 1} + 1 \right]^{-1} \cdot I_M(\tilde{\nu}) \quad (2)$$

where $I_M(\tilde{\nu})$ is the measured normalized Raman intensity at wavenumber $\tilde{\nu}$, $\tilde{\nu}_0$ is the wavenumber of the laser line used and c , h and k_B are, respectively, the velocity of light, Planck's constant and Boltzmann's constant.

2.3. Catalytic evaluation studies

Catalytic tests for CO oxidation were carried out in a quartz fixed-bed reactor (9 mm i.d.), loaded with 400 mg of catalyst. The total flow rate of the feed gas (2000 ppm CO and 1.0 vol.% O₂ in He) was 500 cm³/min, corresponding to a Gas Hour Space Velocity (GHSV) of 39,000 h^{−1}. Catalytic evaluation measurements were carried out by increasing the temperature by 25-degree steps up to 500 °C. The reactant CO was analyzed by using an online CO analyzer (Horiba VIA-510). The CO conversion (X_{CO}, %) was calculated by the following equation:

$$X_{\text{CO}}(\%) = \frac{[\text{CO}]_{\text{in}} - [\text{CO}]_{\text{out}}}{[\text{CO}]_{\text{in}}} \times 100 \quad (3)$$

where [CO]_{in} and [CO]_{out} are the CO concentration (ppm) in the inlet and outlet gas streams, respectively.

3. Results and discussion

3.1. Textural and structural characterization (BET, XRD)

The main textural properties of ceria materials (BET surface area, total pore volume, average pore size diameter) are presented in Table 1. Bare ceria supports exhibit higher BET surface areas compared to Cu/CeO₂ samples. Among them, CeO₂-NP presents the highest BET surface area (109.4 m²/g), followed by CeO₂-NR (91.8 m²/g) and CeO₂-NC (39.5 m²/g). The incorporation of copper into the ceria carrier leads to a decrease in the BET surface area; a reduction percentage of 13–18% in

Table 1
Textural/structural characteristics of bare CeO₂ and Cu/CeO₂ samples.

Sample	BET Analysis			XRD Analysis		XRF Analysis
	BET Surface Area (m ² /g)	Pore Volume (cm ³ /g)	Average Pore Size (nm)	Average crystallite diameter, D _{XRD} (nm) ^a		Cu content (wt. %) ^b
				CeO ₂	CuO	
CeO ₂ -NC	39.5	0.12	12.5	19.2	–	–
CeO ₂ -NR	91.8	0.71	30.9	13.2	–	–
CeO ₂ -NP	109.4	1.04	38.1	9.5	–	–
Cu/CeO ₂ -NC	34.3	0.29	33.4	19.2	52	7.2
Cu/CeO ₂ -NR	75.4	0.40	21.2	11.6	43	7.4
Cu/CeO ₂ -NP	90.7	0.29	12.7	9.6	31	7.6

^a Calculated applying Scherrer Eq. (1).

^b Cu content was determined via a linear calibration line with R² > 0.99 obtained by the analysis of reference copper-ceria samples by XRF.

BET surface area is observed in all cases. The sample with the morphology of nanopolyhedra exhibits the highest BET surface area before and after the incorporation of copper into the ceria support. In particular, the following order regarding the BET surface area of copper-ceria samples is obtained: Cu/CeO₂-NP (90.7 m²/g) > Cu/CeO₂-NR (75.4 m²/g) > Cu/CeO₂-NC (34.3 m²/g). The actual Cu content was determined by XRF analysis for all three samples as ~7.5 wt. % (Table 1).

The XRD patterns of all the samples are shown in Fig. 1. The main peaks can be indexed to (111), (200), (220), (311), (222), (400), (331) and (420) planes of a face-centered cubic fluorite structure of ceria (Fm3m symmetry, no. 225) [47]. The XRD peaks corresponding to CuO crystal phases at 2θ 35.3°, 38.2° and 62° are observed for all the catalysts, indicating heterodispersion or aggregation of copper species on the surface of cerium oxide [48,49].

The average crystallite diameter of CeO₂ and CuO phases were evaluated by XRD diffractions by employing the Scherrer equation

(Table 1). Measurements of the CeO₂ mean particle size resulted in 19.2, 11.6 and 9.6 nm for the Cu/CeO₂-NC, Cu/CeO₂-NR and Cu/CeO₂-NP, respectively. More or less the same crystallite size was calculated for the bare ceria supports, which declare that the addition of copper over ceria does not affect the structural characteristics of the CeO₂ support (see below TEM analysis). Similar crystallite sizes to that obtained here have been recently reported for ceria nanocubes, nanorods and nanopolyhedra prepared by the hydrothermal method [27]. It should be also noted that Cu/CeO₂-NC exhibits the largest ceria crystallite size as well as the smallest BET surface area, leading to the largest CuO particle size and to inferior catalytic performance as will be discussed in the sequence.

Regarding the mean particle size of copper phase the following order was recorded: Cu/CeO₂-NC (52 nm) > Cu/CeO₂-NR (43 nm) > Cu/CeO₂-NP (31 nm), which coincides to that obtained for CeO₂. In view of this fact, it has been reported that the structural characteristics of ceria can determine the particle size of CuO, with direct implications on catalytic activity [27]. Interestingly, the same trend, in relation to Cu particle size vs. ceria morphology (NC, NR, NP), has been recently found for 20 wt.% Cu/CeO₂ catalysts, verifying the present findings [39]. It is also worth mentioning that the crystallite size of both ceria and CuO particles follows the reverse order of BET area (Table 1), implying an agglomeration upon surface area decrease. The same trend was observed by Zabilskiy et al. [14] for nanoshaped Cu/CeO₂ catalysts.

3.2. Redox properties (H₂-TPR)

TPR experiments, employing H₂ as a reducing agent, were carried out to gain insight into the impact of ceria morphology on the redox properties of as-prepared samples. Fig. 2a presents the reduction profiles of the bare CeO₂ samples, which consist of two broad peaks centred at 526–551 °C and 789–813 °C. They have been ascribed to the reduction of surface oxygen (O_s) and bulk oxygen (O_b) of ceria, respectively [28,50,51]. The H₂ consumption which corresponds to surface oxygen and bulk oxygen reduction is presented in Table 2. The CeO₂-NR

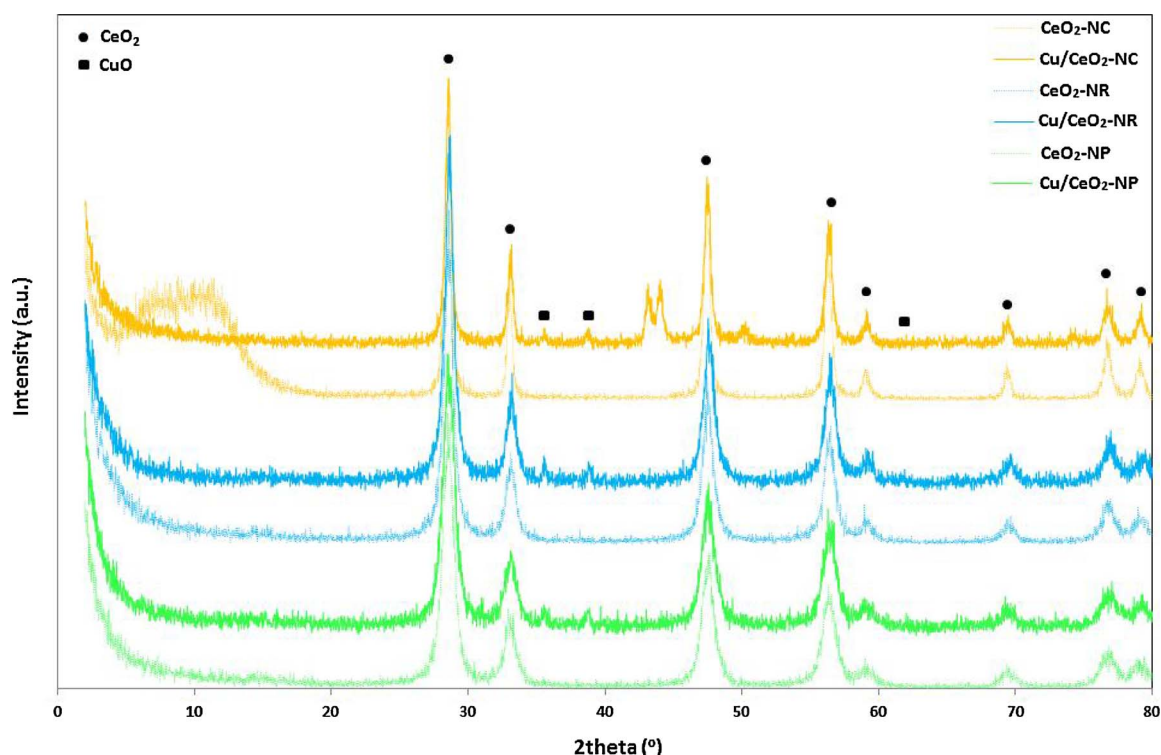


Fig. 1. XRD patterns of bare CeO₂ and Cu/CeO₂ samples; peaks at θ = 42–44° in Cu/CeO₂-NC sample are attributed to interferences from the stainless steel sample holder.

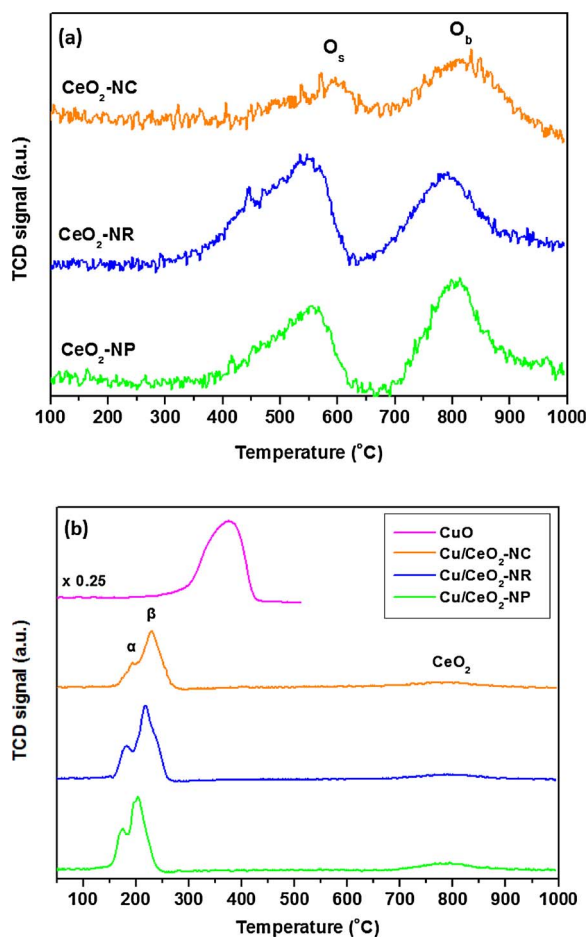


Fig. 2. H₂-TPR profiles of bare CeO₂ (a) and Cu/CeO₂ (b) samples.

Table 2
Redox characteristics of ceria samples.

Sample	H ₂ consumption (mmol H ₂ g ⁻¹)			O _s /O _b ratio	Peak Temperature (°C)	
	O _s peak	O _b peak	Total		O _s peak	O _b peak
CeO ₂ -NP	0.48	0.51	0.99	0.94	555	804
CeO ₂ -NR	0.59	0.52	1.11	1.13	545	788
CeO ₂ -NC	0.41	0.58	0.99	0.71	589	809

exhibits the highest surface-to-bulk oxygen (O_s/O_b) ratio (1.13), followed by CeO₂-NP (0.94) and CeO₂-NC (0.71). These results indicate that CeO₂-NR exhibits the highest population of loosely bound oxygen species, resulting in enhanced reducibility and oxygen mobility, as will be further elaborated below.

It is also worth noticing that CeO₂-NR, and to a lesser extent CeO₂-NP, exhibits a main O_s peak at 550 °C, accompanied by a shoulder at about 450 °C, in contrast to CeO₂-NC which shows one main peak at 589 °C. The latter is in agreement with the lower temperature reduction of {110} and {100} surfaces compared to {111} [14,25,26].

The corresponding reduction profiles of Cu/Ceria samples along with that of a CuO reference sample are depicted in Fig. 2b. In Table 3 the main reduction peaks along with their corresponding H₂ consumption (mmol H₂/g) are summarized. Bare CuO has one reduction peak at 380–392 °C, in accordance to literature [52]. The reduction profiles of all Cu/CeO₂ samples exhibit two overlapping peaks in the range of 176–228 °C, as well as one peak at ca. 793 °C, attributed to the reduction of Ce⁴⁺ into Ce³⁺ [53]. The low-temperature peak (peak α) in the range of 176–194 °C is attributed to the reduction of finely dispersed CuO_x species interacting strongly with the CeO₂ surface [54–56].

Table 3
Redox characteristics of Cu/CeO₂ samples.

Sample	H ₂ consumption (mmol H ₂ g ⁻¹)			Peak Temperature (°C)	
	Peak (α + β)	CeO ₂ peak	Total	Peak α	Peak β
Cu/CeO ₂ -NC	1.50	0.65	2.15	194	228
Cu/CeO ₂ -NP	1.65	0.25	1.90	176	201
Cu/CeO ₂ -NR	1.80	0.25	2.05	181	217

The peak at higher temperature (peak β) is related to larger CuO clusters formed on the ceria surface [52]. It is obvious that the reduction of Cu/CeO₂ samples occurs at considerably lower temperature than those of bare CuO and CeO₂ samples. This is attributed to the “synergistic effect” between the two oxide phases that weakens the metal-oxygen bonds [14,49].

To gain further insight into the impact of support's nature on the reducibility of Cu/CeO₂ samples, the H₂ consumption in the low temperature range, which is related to the reduction of CuO_x species and surface oxygen of ceria, is estimated (Table 3). The following order, in terms of H₂ uptake, is obtained: Cu/CeO₂-NR (1.80 mmol H₂/g) > Cu/CeO₂-NP (1.65 mmol H₂/g) > Cu/CeO₂-NC (1.50 mmol H₂/g). These results indicate the superior reducibility of Cu/CeO₂-NR. Notably, the reduction order of the supported catalysts is perfectly related to that of bare ceria supports indicating the key role of support morphology on the reducibility of Cu/CeO₂ catalysts. It is also worth noticing that the amount of H₂ required for the reduction of Cu/Ceria samples always surpasses the theoretical amount of H₂ for the complete reduction of CuO to Cu (~1.34 mmol H₂/g on the basis of a Cu nominal loading of 8.5 wt.%).

The present TPR results clearly indicate: (i) the enhanced reducibility of mixed oxides compared to bare ones, and (ii) the significant impact of ceria nanostructure on the redox properties of Cu/CeO₂ binary oxides. These findings can be interpreted in terms of Cu-Ceria interactions, which in turn facilitate the reduction of ceria capping oxygen. In particular, the superior reducibility of mixed oxides can be ascribed to: (i) the hydrogen spillover from Cu sites to ceria carrier, (ii) the electronic metal-support interactions (EMSI) between copper and ceria particles, which directly affect the reducibility of CeO₂ [33]. In view of this fact, a relationship between the reduction temperature of ceria and the work function of metal dopants has been established [57]. Interestingly, in the present work, significant variations on the reducibility of Cu/Ceria binary oxides can be induced by altering the ceria morphology instead the nature of active phase, implying a different extent of metal-support interactions. These findings will be further interpreted on the basis of XPS and Raman results (*vide infra*).

3.3. Surface analysis (XPS)

XPS analysis was conducted to assess the impact of ceria morphology on elementary oxidation states of bare CeO₂ and Cu/CeO₂ samples. Fig. 3a shows the Ce 3d XPS spectra of all the samples, which can be resolved to eight components, as reported in several relevant studies [39,55,58–64]. The Ce 3d spectrum consists of two series of spin-orbit lines u and v. Ce 3d_{3/2} spin-orbit components which correspond to u lines include three characteristic peaks labeled as u (900.7 eV), u' (907.6 eV) and u'' (916.4 eV). Ce 3d_{5/2} spin-orbit components which correspond to the series of v lines contain the three peaks labeled as v (882.2 eV), v' (888.8 eV) and v'' (898.2 eV). These three pairs of peaks are attributed to the characteristic peaks of Ce⁴⁺. Moreover, the residual two spectral lines labeled as u' (902.1 eV) and v' (883.8 eV) belong to the Ce³⁺ species. The proportion of Ce³⁺ ions with regard to the total cerium is calculated from the area ratio of the sum of the Ce³⁺ species to that of the total cerium species [55]. Table 4 shows that bare ceria samples have a similar amount of Ce³⁺ varying between 23.3 and 25.3%. Regardless of the number of defect sites in the

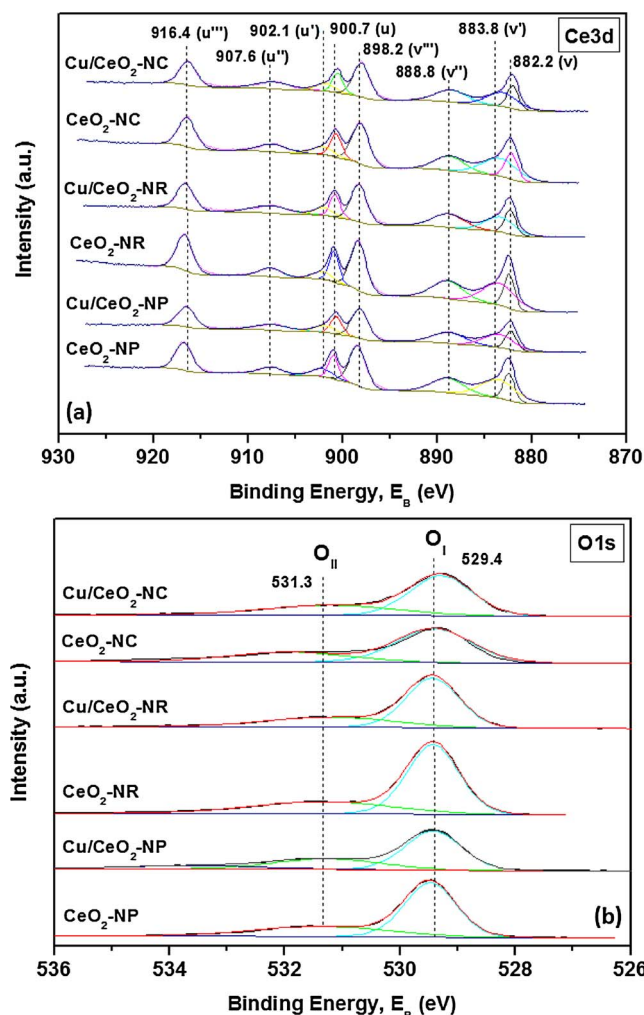


Fig. 3. XPS spectra of Ce 3d (a) and O 1s (b) of bare CeO₂ and Cu/CeO₂ samples.

Table 4
XPS results for bare CeO₂ and Cu/CeO₂ samples.

Sample	XPS					Cu/Ce atomic ratio
	O _I (%)	O _{II} (%)	O _I /O _{II}	Ce ³⁺ (%)	Cu ⁺ (%)	
CeO ₂ -NC	66.5	33.5	1.99	23.3	–	–
CeO ₂ -NR	68.1	31.9	2.13	24.3	–	–
CeO ₂ -NP	67.1	32.9	2.04	25.3	–	–
Cu/CeO ₂ -NC	65.4	34.6	1.89	21.9	11.8	0.16
Cu/CeO ₂ -NR	66.9	33.1	2.02	23.9	16.1	0.18
Cu/CeO ₂ -NP	66.2	33.8	1.96	23.3	13.0	0.35

bulk of ceria, it has been found that ceria samples of various morphologies can exhibit similar Ce 3d spectra profiles [16,65]. The same similarity is observed for copper-ceria samples as well, in which the amount of Ce³⁺ varies between 21.9 and 23.9%, with the CeO₂-NR exhibiting the highest population of Ce³⁺ species. Despite the preparation methods and the presence of copper, it has been shown that there is no significant differences in the amount of reduced, non-stoichiometric cerium species, in the external layers of the catalysts [66]. However, the uncertainty in precise Ce³⁺ determination by XPS, due to high-vacuum conditions and X-ray irradiation, should be mentioned [67].

The corresponding O 1s XPS spectra are illustrated in Fig. 3b. There are two characteristic peaks in the O 1s spectra of all the catalysts. The primary band (529.4 eV) denoted as O_I represents the lattice oxygen

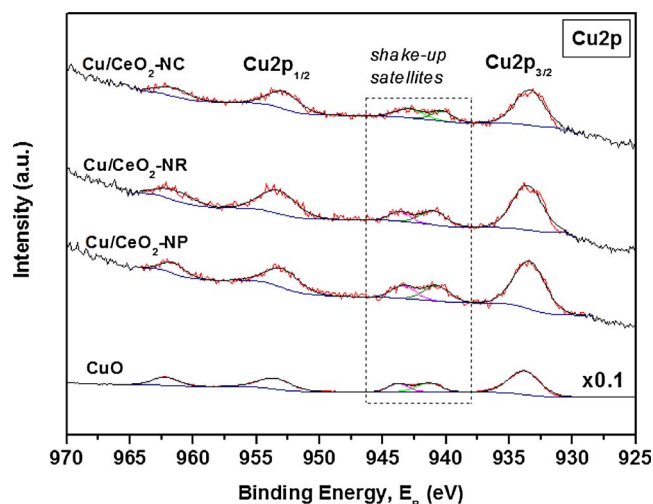


Fig. 4. Cu 2p XPS spectra of CuO and Cu/CeO₂ samples.

bound to CuO and CeO₂ phases, while the shoulder at 531.3 eV is attributed to chemisorbed oxygen peak (O_{II}) including adsorbed oxygen (O[−]/O₂^{2−}), adsorbed water, hydroxyl and carbonate species. For the bare ceria samples, the following order, in terms of the O_I/O_{II} ratio, is obtained: CeO₂-NR (2.13) > CeO₂-NP (2.04) > CeO₂-NC (1.99) which is perfectly matched to the order of their catalytic performance, indicating the key role of lattice oxygen on the CO oxidation performance, as will be discussed below. Exactly the same trend is obtained for copper-ceria samples, i.e.: Cu/CeO₂-NR (2.02) > Cu/CeO₂-NP (1.96) > Cu/CeO₂-NC (1.89), implying again the key role of support morphology on oxygen mobility/reduction. These findings along with the TPR results corroborate that the samples with the rod-like morphology, namely CeO₂-NR and Cu/CeO₂-NR, demonstrate the highest population of loosely bound oxygen species, resulting in improved reducibility and oxygen kinetics.

Fig. 4 shows the Cu 2p XPS spectra of Cu/CeO₂ samples. For comparison purposes the spectrum of CuO reference sample is also depicted. All spectra are characterized by two main peaks of Cu 2p_{1/2} (953.7 eV) and Cu 2p_{3/2} (933.8 eV), as well as shake-up satellite peaks at 943 eV, which are typical characteristics of Cu²⁺ species [31,55,64]. The latter is further confirmed by the XPS spectrum of CuO reference sample.

It should be mentioned here that Cu⁺/Cu₂O and Cu²⁺/CuO species cannot be easily resolved because of the proximity in their binding energies [55]. In this regard, the discrimination of Cu oxidation state is usually performed by the comparison of Cu 2p binding energy and Auger parameters in Wagner plots. However, the difficulty to precisely discriminate Cu oxidation states even by means of XPS positions and Auger parameters has been documented [31,68,69]. In light of the above, the determination of the relative population of Cu⁺ species is performed here on the basis of a well-established procedure, according to the following equation [64,70,71]:

$$\%Cu^{+} = (A - (A_1/B)B)/(A + B) \times 100 \quad (4)$$

3/2

Table 4 lists the relative content of Cu⁺ species on Cu/Ceria samples. Cu/CeO₂-NR exhibits the highest concentration (16.1%) followed by Cu/CeO₂-NP (13.0%) and Cu/CeO₂-NC (11.8%). This sequence conforms with the order of O_s/O_b ratio (Table 2) and reducibility (Table 3), justifying the close relationship between redox and electronic properties established through metal-support interactions. In complete agreement, it has been found that the strong interaction of CuO_x species with rod-like ceria supports can lead to a stable existence of Cu⁺ species in Cu/Ceria samples [55]. Moreover, the same Cu⁺ trend, in relation to nanoceria morphology (rods, cubes, polyhedra), was recently revealed for 10 wt. % Cu/CeO₂ catalysts [27].

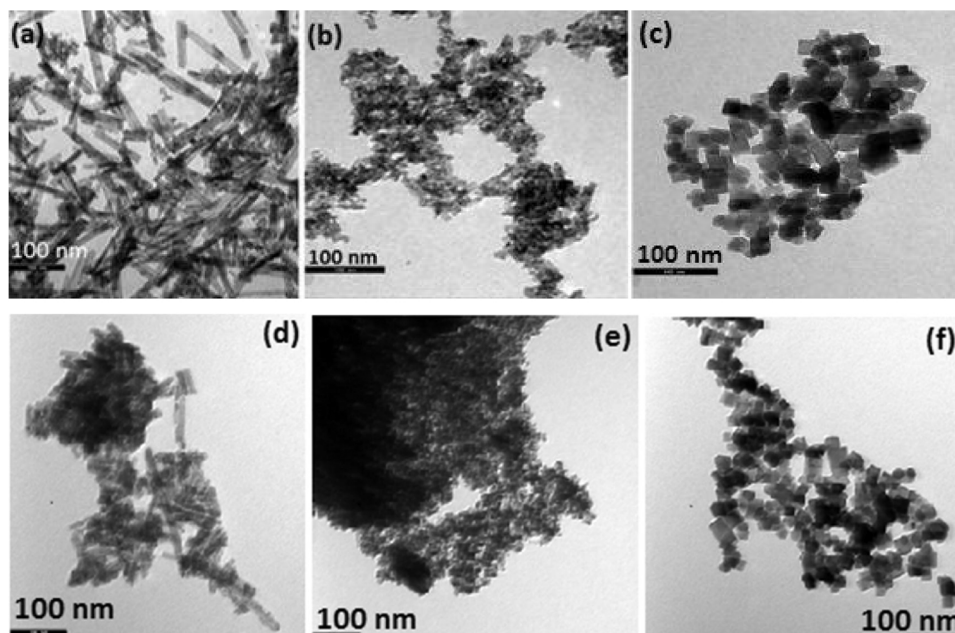


Fig. 5. TEM images of the samples: (a) CeO₂-NR, (b) CeO₂-NP, (c) CeO₂-NC, (d) Cu/CeO₂-NR, (e) Cu/CeO₂-NP and (f) Cu/CeO₂-NC.

Regarding the Cu distribution to the outer surface, both copper-ceria nanocubes and nanorods exhibit similar values of Cu/Ce surface atomic ratio (0.16 and 0.18, respectively, Table 4), which however is slightly lower to the nominal one (0.25), implying an impoverishment of catalyst surface to copper. On the other hand, in nanopolyhedra the Cu/Ce atomic ratio is almost double (0.35) and higher than the theoretical implying an enrichment of catalyst surface to copper, in accordance to literature [39].

3.4. Morphological characterization (TEM)

In order to gain insight into the effect of hydrothermal synthesis on the morphological characteristics of ceria nanoparticles, transmission electron microscopy (TEM) studies were also carried out. Fig. 5(a–c) depicts the images of bare ceria samples. CeO₂-NR (Fig. 5a) shows the presence of a rod-like morphology. The rods' length varies from 25 to 200 nm. Fig. 5b and c demonstrates mostly nanopolyhedra of irregular shapes and cubes, respectively. Fig. 5(d–f) illustrate the TEM images of copper-ceria samples. It is evident that the incorporation of copper into the ceria lattice does not affect the morphology of the support.

3.5. Structure of anionic sub-lattice and redox properties of CeO₂ polymorphs probed by *in situ* Raman spectroscopy

Fig. 6 shows the *in situ* steady-state Raman spectra obtained for the CeO₂-NR, CeO₂-NP and CeO₂-NC samples at 440 °C under flowing 20% O₂/He gas, *i.e.* under oxidizing conditions. The characteristic F_{2g} mode due to the $Fm\bar{3}m$ fluorite cubic ceria structure observed at 457 cm⁻¹ prevails in all spectra. Additionally, as reported previously [16,46,72], a weak band at ~260 cm⁻¹ (due to second order transverse acoustic mode) and the so-called defect-induced band (band “D”) at ~600 cm⁻¹ “leak” as result of relaxation of symmetry selection rules caused by structural perturbations of the ceria cubic lattice. The intensity of the “D” band is a measure of the deformation of the anionic lattice that leads to punctual defects and O vacancies. Thus the $I_D/I_{F_{2g}}$ ratio is commensurate to the abundance of structural defects [46]. The anionic lattice of bare ceria is known to be deformed due to O atoms' relocation from the interior of tetrahedral cationic sub-lattice sites to the interior of ideally empty octahedral cationic sites (Frenkel interstitial sites) [73].

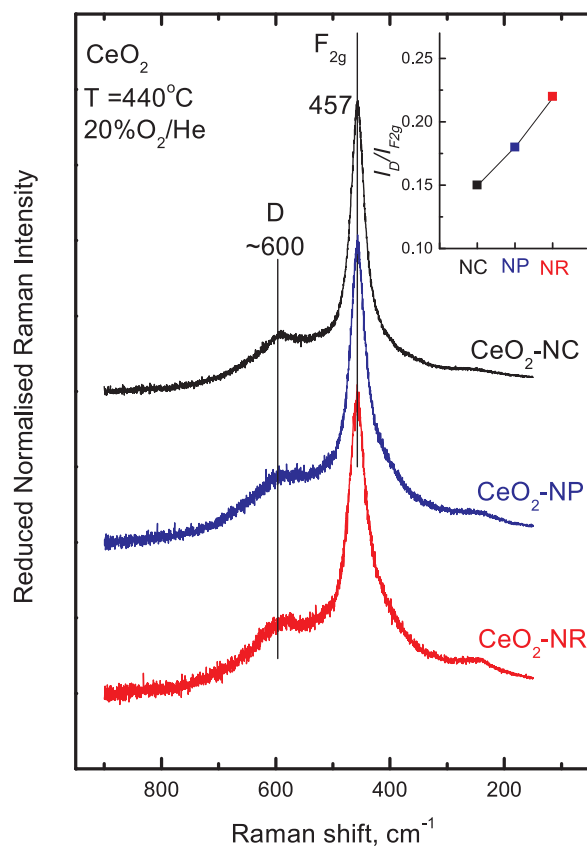


Fig. 6. *In situ* Raman spectra obtained for CeO₂ (NR, NP and NC as indicated by each spectrum). Inset: intensity ratio $I_D/I_{F_{2g}}$. Laser wavelength, $\lambda_0 = 491.5$ nm; laser power, $w = 25$ mW; spectral slit width, 6 cm⁻¹.

Previously, we had demonstrated that the “D” band is comprised of at least two components, “D1” (above 600 cm⁻¹) and “D2” (below 600 cm⁻¹) [46,72]. Sequential *in situ* steady-state Raman spectra under alternating oxidizing and reducing flowing gas at 450 °C were adequate to demonstrate that band D1 is due to Ce–O modes involving O atoms

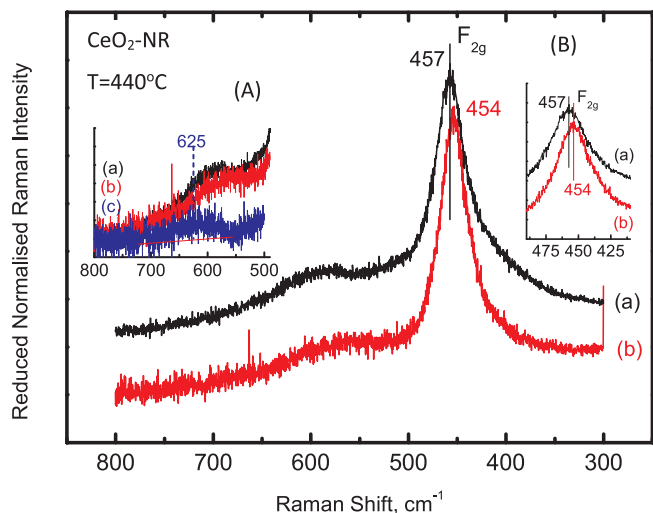


Fig. 7. *In situ* sequential Raman spectra obtained for CeO₂-NR: (a) under flowing 20%O₂/He; (b) under flowing 5%H₂/He. Insets: (A) trace (c) obtained after subtracting trace (b) from trace (a); (B) focus on the spectral region of the F_{2g} band. Recording parameters: see Fig. 6 caption.

that are relatively loosely bound (e.g. in Frenkel interstitial sites) and can be detached under the applied reducing conditions at 450 °C, whereas band D2 is due to vibrational modes within coordinatively unsaturated sites (e.g. MO₇) and remains unaffected under reducing conditions at 450 °C [46].

Clearly (as seen in Fig. 6 inset) a higher abundance of defects (evidenced by the pertinent relative $I_D/I_{F_{2g}}$ ratios shown in arbitrary scale) is observed for the CeO₂-NR polymorph and the actual trend, i.e. CeO₂-NR > CeO₂-NP > CeO₂-NC agrees with the aforementioned results as well as with the redox and catalytic activity results discussed below.

Figs. 7–9 show the *in situ* steady-state sequential Raman spectra obtained at 440 °C for CeO₂-NR (Fig. 7), CeO₂-NP (Fig. 8) and CeO₂-NC (Fig. 9) under oxidizing atmosphere (after treatment for 1 h under flowing 20%O₂/He; spectra marked by (a)) and under reducing atmosphere (after treatment for 1 h and 45 min under flowing 5%H₂/He; spectra marked by (b)). In agreement to our recent detailed report [46], it is evidenced (see insets (A) in Figs. 7–9 focusing in the region of the “D” band) that under reducing conditions, the “D” band at ~600 cm⁻¹

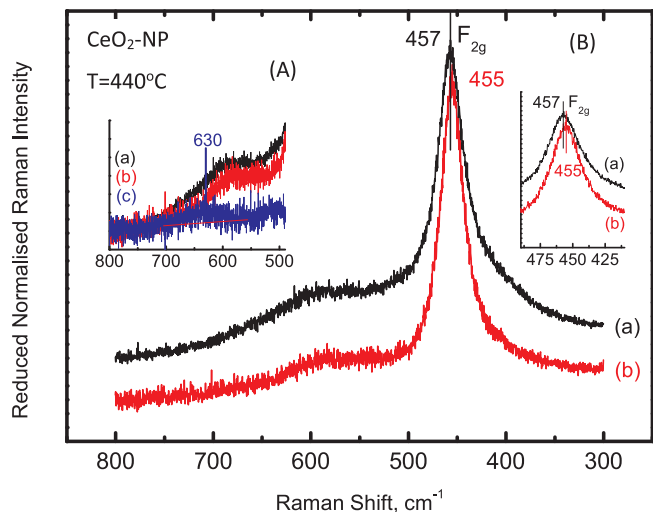


Fig. 8. *In situ* sequential Raman spectra obtained for CeO₂-NP: (a) under flowing 20%O₂/He; (b) under flowing 5%H₂/He. Insets: (A) trace (c) obtained after subtracting trace (b) from trace (a); (B) focus on the spectral region of the F_{2g} band. Recording parameters: see Fig. 6 caption.

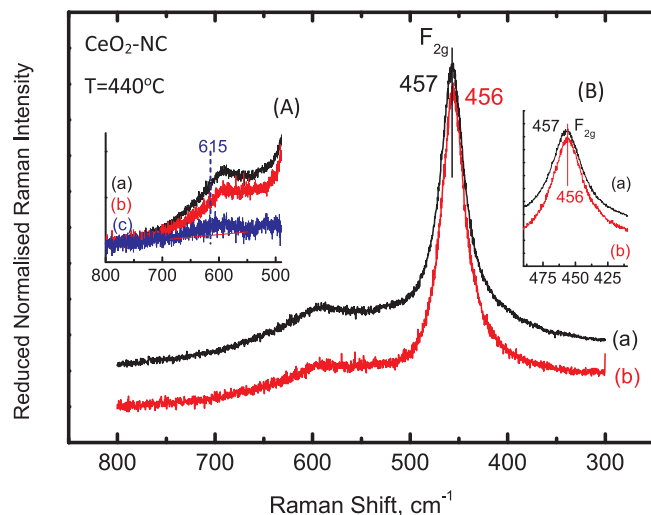


Fig. 9. *In situ* sequential Raman spectra obtained for CeO₂-NC: (a) under flowing 20%O₂/He; (b) under flowing 5%H₂/He. Insets: (A) trace (c) obtained after subtracting trace (b) from trace (a); (B) focus on the spectral region of the F_{2g} band. Recording parameters: see Fig. 6 caption.

loses intensity on its high wavenumber side, namely D1, thereby indicating that the Frenkel O interstitials are loosely bound and can be delivered under the applied reducing conditions. By subtracting spectra (b) from their counterpart spectra (a) we obtain the spectroscopic fingerprint of the detached O atoms (traces (c) in insets (A), Figs. 7–9), as established recently [46,72]. Remarkably, the intensity of the difference band in traces (c) seem to follow the order CeO₂-NR > CeO₂-NP > CeO₂-NC, thereby corroborating the corresponding reducibility sequence evidenced independently by H₂-TPR.

Additionally, the F_{2g} band undergoes a slight red shift under reducing conditions (see insets (B) in Figs. 7–9 that focus on the spectral region of the F_{2g} band). The observed red shift is justified by a partial Ce⁴⁺ → Ce³⁺ reduction that results in lattice expansion due to the higher ionic radius of Ce³⁺ compared to Ce⁴⁺ (i.r._{Ce³⁺}, CN=8 = 1.13 Å > i.r._{Ce⁴⁺}, CN=8 = 0.97 Å) along with a probable particle size decrease, with both effects contributing to a slight red shift. Notably, this effect also follows the same trend, i.e. CeO₂-NR > CeO₂-NP > CeO₂-NC, thereby indicating a higher susceptibility for the CeO₂-NR polymorph to reducing conditions.

Previously [46], we had demonstrated by *in situ* Raman spectroscopy that CeO₂ and CeO₂-ZrO₂ based materials undergo a reversible temperature dependence of their anionic sub-lattice structure, which is indicative of a corresponding reversible temperature dependence of their defect topologies. Accordingly, in the present work, following successive reduction/oxidation cycles, the anionic sub-lattice structure is fully reinstated after treating the CeO₂-NR, CeO₂-NP and CeO₂-NC samples under flowing 20%O₂/He gas at 440 °C for 30 min.

3.6. CO oxidation

The oxidation of CO was employed as a model reaction in order to reveal the impact of ceria morphology on the catalytic performance of both ceria and Cu/Ceria samples. Fig. 10 shows the conversion of CO as a function of temperature for both CeO₂ and Cu/CeO₂ samples. Obviously, the support morphology affects enormously the catalytic activity. In particular, the following oxidation performance, in terms of half-conversion temperature (T₅₀), was obtained: CeO₂-NR (320 °C) > CeO₂-NP (350 °C) > CeO₂-NC (385 °C). The incorporation of copper into the ceria lattice considerably improves the catalytic activity without, however, affecting the activity order: Cu/CeO₂-NR (72 °C) > Cu/CeO₂-NP (83 °C) > Cu/CeO₂-NC (92 °C). Apparently, the Cu/CeO₂ sample with the rod-like morphology exhibits an excellent

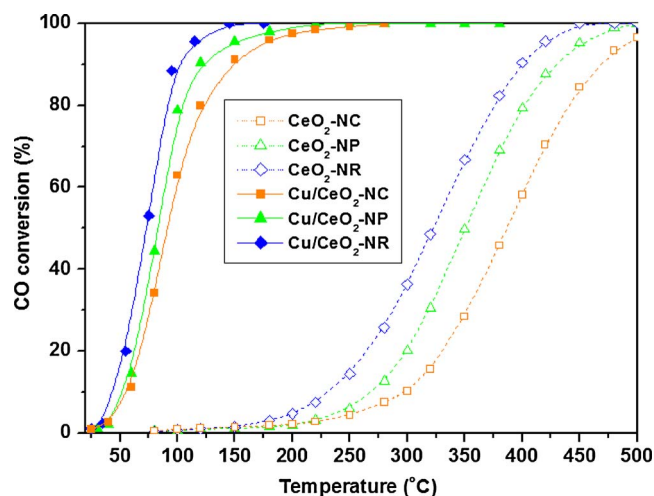


Fig. 10. CO conversion as a function of temperature for Ceria and Cu/Ceria samples of different morphology (NR, NC and NP, as indicated in each curve). Reaction conditions: 2000 ppm CO, 1 vol.% O₂, GHSV = 39,000 h⁻¹.

catalytic performance, offering almost complete CO elimination at temperatures as low as 100 °C. It is also worth noticing that a stable conversion performance (100%) was obtained at 150 °C during a short term (12 h) stability test (not shown for brevity). Moreover, BET and XRD characterization studies over the spent Cu/CeO₂-NR catalysts (after subjected to activity and stability tests) revealed no textural/structural modifications; the mean crystallite size of ceria is slightly increased to 13 nm as compared to 11.6 nm of fresh sample whereas the BET surface area remained almost unchanged (72.8 m²/g as compared to 75.4 m²/g of fresh sample, Table 1). These findings are in agreement with the structural stability of ceria samples upon subsequent oxidation/reduction processes during Raman analysis, further corroborating the reliability of the obtained structure – activity relationships (*vide infra*).

The present findings can be rationalized on the basis of a Mars-van Krevelen, redox type mechanism, well documented in the literature [38,74–78], which mainly involves the following steps, schematically illustrated in Fig. 11:

- i Chemisorption of CO on Cu⁺ active sites towards the formation of Cu⁺-CO species,
- ii Migration of the chemisorbed CO to the metal-support interface,
- iii O₂ activation on the oxygen vacancies of CeO₂ and formation of active oxygen (e.g. O₂⁻) or lattice oxygen (e.g. O²⁻) species,
- iv Reaction between the chemisorbed CO at interface and nearby active oxygen and

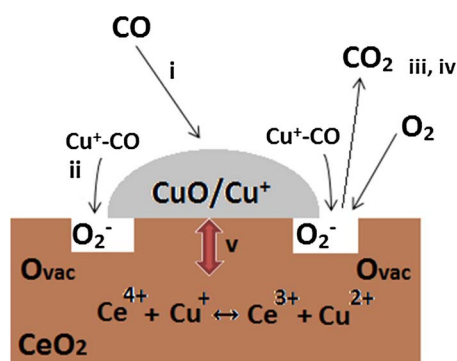
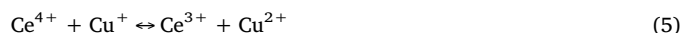


Fig. 11. Schematic illustration of CO oxidation mechanism on Cu/CeO₂ catalysts.

- v Regeneration of Cu⁺ sites and refill of oxygen vacancies by gas phase oxygen involved in consecutive catalytic cycles.

The above mechanistic scheme clearly reveals the key role played by the redox properties of the support and by its interaction with the copper species. In particular, the improved oxygen kinetics/reducibility of ceria carrier facilitates the formation of active oxygen species, whereas the copper-ceria interactions could be considered responsible for the formation of Cu⁺ active species, through the redox equilibrium:



Both factors are crucial towards a high oxidation performance.

In view of the above, the superiority of Cu/CeO₂-NR, exposing CeO₂-{100}/{110} facets, can receive a consistent explanation. The improved reducibility and oxygen exchange kinetics of ceria nanorods, linked to their abundance in defects and O vacancies, can be considered as the decisive factors for the enhanced catalytic performance. In a similar manner, the improved CO oxidation performance of Pd supported on ceria nanorods as compared to different ceria morphologies was ascribed to the low oxygen vacancy formation energy, strong reducibility and high surface oxygen mobility [79]. Moreover, the superior carbonate hydrogenation activity of Cu/CeO₂ nanorods as compared to nanocubes and nanoparticles has been attributed to the high reactivity of {110} and {100} planes towards a better balance of defect topology and number of oxygen vacancies followed by Cu⁺ species stabilization, rather to particle size effects [39].

The above arguments regarding structure-function relationships are fully supported by the perfect relationships between the catalytic performance and the surface-to-bulk ratio (O_s/O_b) (Fig. 12a), as well as the Cu⁺ percentage derived by XPS measurements (Fig. 12b). More importantly, the *in situ* Raman measurements, more closely reflecting the catalyst state under working conditions, corroborate the above arguments by demonstrating that the relative abundance of defects and O vacancies exhibited by the I_D/I_{FG} intensity ratios (Fig. 6) as well as the relative reducibility expressed by the detachment of O atoms and the partial Ce⁴⁺ → Ce³⁺ reduction (the latter one exhibited by the red shift of the F_{2g} mode) under flowing H₂ gas (Figs. 7–9) follow the same trends with the catalytic performance of bare and Cu-doped ceria, thereby demonstrating the key role of the support. Accordingly, a relationship between the catalytic performance (T₅₀) and the relative abundance of structural defects was also established (Fig. 12c). In a similar manner, a relationship between the abundance of structural defects of copper-ceria catalysts and their CO oxidation activity was recently observed [80].

Similar to the aforementioned structure-property relationships can be obtained by taking into account the CO conversion (%) or CO consumption rate (r_{CO}, nmol s⁻¹ g⁻¹) at differential conditions (GHSV = 39,000 h⁻¹, X_{CO} < 25%), which can rereflect more accurately the impact of reaction conditions and mixed oxides intrinsic properties on the catalytic performance (Table 5).

In summary, the samples with the rod-like morphology exhibit the highest concentration of weakly bound oxygen species which are related to oxygen mobility and the formation of oxygen vacancies. In addition, ceria nanorods seem to facilitate the formation of Cu⁺ active species through the Cu²⁺/Cu⁺ and Ce⁴⁺/Ce³⁺ redox equilibrium (eq. 5), in agreement with literature [27]. It should be noted, however, that no strong evidences, in relation to Cu⁺ abundance under reaction conditions, can be obtained on the basis of the present *ex situ* XPS studies. Definitive conclusions regarding the role of support morphology on the local surface chemistry under reaction conditions can be obtained by means of sophisticated characterization techniques (e.g., *in situ* time-resolved X-ray absorption near-edge spectroscopy (TR-XANES)).

It is also worth mentioning that the rod-like samples, despite their inferior textural (surface area) and structural (crystallite size)

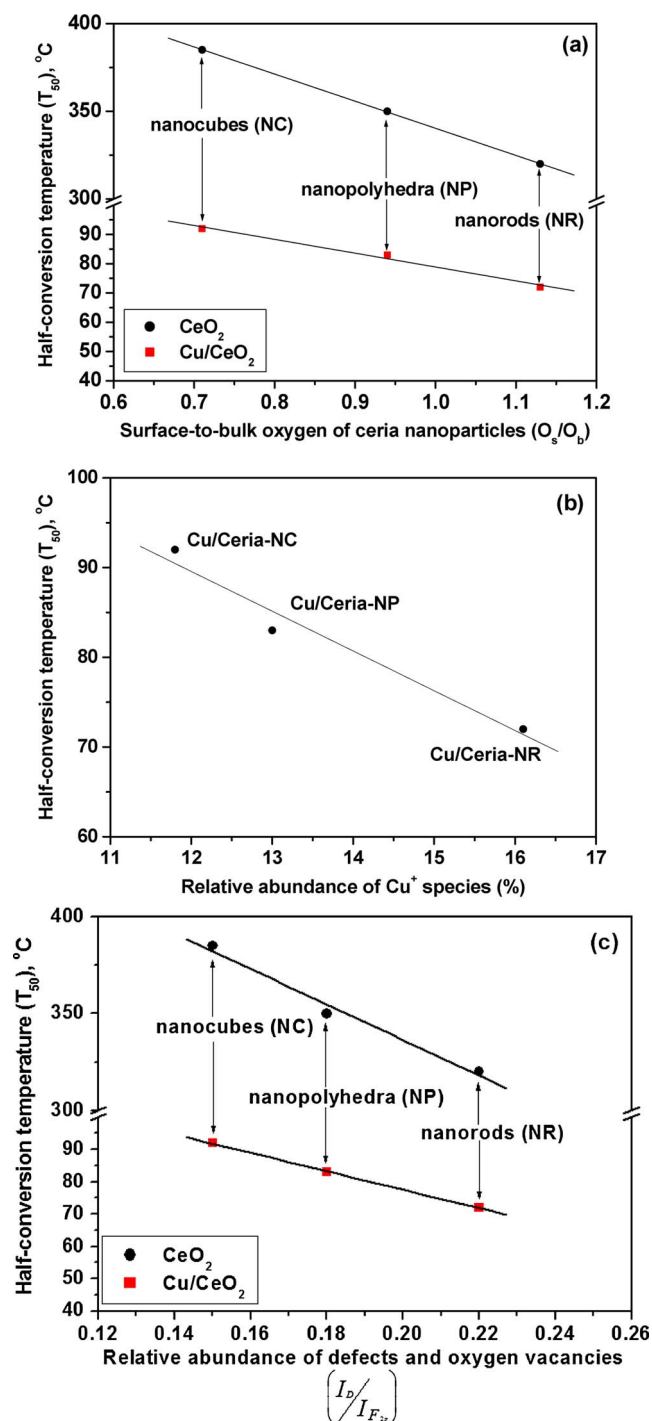


Fig. 12. Relationship between the half-conversion temperature (T_{50}) and the O_s/O_b TPR ratio (a), Cu^+ percentage derived by XPS (b) and the relative intensity ratio of $I_D/I_{F_{2g}}$ (c).

Table 5
Conversion performance and specific activity of Cu/Ceria samples^a.

Sample	Conversion performance		Specific activity at 60 °C	
	T_{50} ^b	X_{CO} ^c	nmol s ⁻¹	nmol s ⁻¹ g ⁻¹
Cu/CeO ₂ -NC	92	11	75	188
Cu/CeO ₂ -NP	83	17	116	289
Cu/CeO ₂ -NR	72	25	171	425

^a Reaction conditions: 2000 ppm CO, 1 vol.% O₂, GHSV = 39,000 h⁻¹.

^b Required temperature for 50% CO conversion.

^c CO conversion at 60 °C.

characteristics compared to polyhedral samples, exhibited the highest catalytic performance. The latter points to the crucial role of exposed facets, rather than structural/textural characteristics, towards the determination of catalytic activity, as previously discussed.

On the other hand, ceria defects and imperfections – linked to its morphology – could affect the particle size and dispersion of active phase, thereby implying the interrelation between size and shape effects [36]. In addition, the key role of particle size itself on metal-support interactions has been well documented [33]; bonding interactions between metal particles of nanometer size down to single atoms can directly result in strong electronic perturbations (EMSI effect) with great consequences in catalysis. Nevertheless, as the size of the interacting particles increases the role of support is limited to particle's perimeter or interfacial atoms.

In view of the above perspectives, the superior catalytic performance of Cu/Ceria-NR could be more precisely ascribed to the co-adjustment of interrelated geometric (size) and morphological (shape) characteristics. Nonetheless, the development of model mixed oxides of well-defined morphology and size is a prerequisite in order to gain insight into the distinct role of shape and size.

4. Conclusions

Three nanostructures of ceria with different exposed facets, *i.e.*, nanorods (NR), nanocubes (NC) and nanopolyhedra (NP), were synthesized by the hydrothermal method and employed as supporting carriers of the Cu phase. Catalytic evaluation studies, employing the CO oxidation as probe reaction, revealed the following activity order: CeO_2 -NR > CeO_2 -NP > CeO_2 -NC. Incorporation of Cu to different ceria supports boosts the catalytic performance without, however, affecting the sequence observed for bare ceria. A characterization study by means of complementary *ex situ* and *in situ* characterization techniques was employed to gain insight into the underlying mechanism of observed differences. The results clearly revealed the key role of ceria morphology on the structural defects and oxygen mobility, following the sequence: NR > NP > NC. The superiority of Cu/Ceria samples with a rod-like morphology can be well rationalized on the basis of a Mars-van Krevelen type of mechanism, involving adsorption of CO on Cu^+ species and O₂ activation on oxygen vacancies, whereas copper-ceria interactions can facilitate the regeneration of active sites. The Cu/Ceria-NR with {100} and {110} reactive planes exhibited the best catalytic performance ($T_{50} = 72$ °C) due to its improved surface/redox properties. Notably, a perfect relationship between the catalytic performance and the following parameters was established: i) abundance of loosely bound oxygen species (TPR), ii) relative population of partial reduced Cu^+/Ce^{3+} redox pairs (XPS/Raman), iii) relative abundance of defects and O vacancies as evidenced by the *in situ* Raman results. Despite the inferior textural and structural characteristics of nanorods as compared to polyhedral samples, the former exhibited the highest catalytic performance, revealing the key role of exposed crystal planes. The present findings demonstrate that the rational design of metal/oxides combinations of well-defined size and shape could offer a platform for a wide range of materials with real life energy and environmental applications.

Author contributions

M.L. contributed to materials synthesis, results interpretation and paper writing. E.P. and E.I. contributed to catalytic evaluation and characterization (BET, XRD) studies. S.A.C. contributed to materials characterization (TPR, XPS, TEM). N.K. contributed to materials synthesis and XRF analysis. C.A. contributed to the Raman measurements. S.B. performed the Raman analysis, contributing also to results interpretation and paper writing. M.K. contributed to the conception, design, results interpretation and writing of the paper. All authors contributed to the discussion, read and approved the final version of the

manuscript.

Acknowledgments

The present work is financially supported by the General Secretariat for Research and Technology (GSRT) and the Hellenic Foundation for Research and Innovation (HFRI). SACC thanks Fundação para a Ciência e Tecnologia (FCT) for financial support through Investigator FCT program (IF/01381/2013/CP1160/CT0007), with financing from the European Social Fund and the Human Potential Operational Program. This work was partially supported by Project POCI-01-0145-FEDER-006984 – Associate Laboratory LSRE-LCM funded by FEDER through COMPETE2020 – Programa Operacional Competitividade e Internacionalização (POCI) – and by national funds through FCT. MK is thankful for the Greece–Portugal Bilateral Educational Programme. Authors are thankful to Dr. Carlos M. Sá (CEMUP) for assistance with XPS analyses and to Dr. Pedro Tavares and Dr. Lisete Fernandes (UME/CQVR/UTAD) for assistance with the TEM analyses.

References

- [1] J. Paier, C. Penshke, J. Sauer, *Chem. Rev.* 113 (2013) 3949–3985.
- [2] C. Sun, D. Xue, *Phys. Chem. Chem. Phys.* 15 (2013) 14414–14419.
- [3] T. Montini, M. Melchionna, M. Monai, P. Fornasiero, *Chem. Rev.* 116 (2016) 5987–6041.
- [4] S.W. Yu, H.H. Huang, C.W. Tang, C. Bin Wang, *Int. J. Hydrogen Energy* 39 (2014) 20700–20711.
- [5] W.-X. Tang, P.-X. Gao, *MRS Commun.* 6 (2016) 311–329.
- [6] D. Zhang, X. Du, L. Shi, R. Gao, *Dalton Trans.* 41 (2012) 14455–14475.
- [7] S.A. Mock, S.E. Sharp, T.R. Stoner, M.J. Radetic, E.T. Zell, R. Wang, *J. Colloid Interface Sci.* 466 (2016) 261–267.
- [8] M. Monte, G. Munuera, D. Costa, J.C. Conesa, A. Martínez-Arias, *Phys. Chem. Chem. Phys.* 17 (2015) 29995–30004.
- [9] T.X.T. Sayle, F. Caddeo, X. Zhang, T. Sakthivel, S. Das, S. Seal, S. Ptasińska, D.C. Sayle, *Chem. Mater.* 28 (2016) 7287–7295.
- [10] X. Yao, F. Gao, Q. Yu, L. Qi, C. Tang, L. Dong, Y. Chen, *Catal. Sci. Technol.* 3 (2013) 1355.
- [11] Z.A. Qiao, Z. Wu, S. Dai, *ChemSusChem* 6 (2013) 1821–1833.
- [12] L.P. Matte, A.S. Kilian, L. Luza, M.C.M. Alves, J. Morais, D.L. Baptista, J. Dupont, F. Bernardi, *J. Phys. Chem. C* 119 (2015) 26459–26470.
- [13] M. Zabilskiy, P. Djinić, E. Tchernychova, A. Pintar, *Appl. Catal. B: Environ.* 197 (2016) 146–158.
- [14] M. Zabilskiy, P. Djinić, E. Tchernychova, O.P. Tkachenko, L.M. Kustov, A. Pintar, *ACS Catal.* 5 (2015) 5357–5365.
- [15] R.K. Singha, A. Shukla, A. Yadav, L.N. Sivakumar Konathala, R. Bal, *Appl. Catal. B: Environ.* 202 (2017) 473–488.
- [16] Z. Wu, M. Li, J. Howe, H.M. Meyer, S.H. Overbury, *Langmuir* 26 (2010) 16595–16606.
- [17] D. Mukherjee, B.M. Reddy, *Catal. Today* (2017), <http://dx.doi.org/10.1016/j.cattod.2017.06.017> Article in press.
- [18] M. Melchionna, P. Fornasiero, *Mater. Today* 17 (2014) 349–357.
- [19] M. Cargnello, V.V.T. Doan-Nguyen, T.R. Gordon, R.E. Diaz, E.a. Stach, R.J. Gorte, P. Fornasiero, *C.B. Murray, Science* 341 (2013) 771–773 (80-).
- [20] G. Vilé, S. Colussi, F. Krumeich, A. Trovarelli, J. Pérez-Ramírez, *Angew. Chem.—Int. Ed.* 53 (2014) 12069–12072.
- [21] K. Mudiyansele, S.D. Senanayake, L. Faria, S. Kundu, A.E. Baber, J. Graciani, A.B. Vidal, S. Agnoli, J. Evans, R. Chang, S. Axnanda, Z. Liu, J.F. Sanz, P. Liu, J.A. Rodriguez, D.J. Stacchiola, *Angew. Chem.—Int. Ed.* 52 (2013) 5101–5105.
- [22] A. Trovarelli, J. Llorca, *ACS Catal.* 7 (2017) 4716–4735.
- [23] K. Wu, L.D. Sun, C.H. Yan, *Adv. Energy Mater.* 6 (2016) 1600501.
- [24] L. Soler, A. Casanovas, A. Urrich, I. Angurell, J. Llorca, *Appl. Catal. B: Environ.* 197 (2016) 47–55.
- [25] L. Liu, Z. Yao, Y. Deng, F. Gao, B. Liu, L. Dong, *ChemCatChem* 3 (2011) 978–989.
- [26] B. Ouyang, W. Tan, B. Liu, *Catal. Commun.* 95 (2017) 36–39.
- [27] Z. Ren, F. Peng, J. Li, X. Liang, B. Chen, *Catal. Today* 7 (2017) 48.
- [28] M. Lykaki, E. Pachatouridou, E. Iliopoulou, S.A.C. Carabineiro, M. Konsolakis, *RSC Adv.* 7 (2017) 6160–6169.
- [29] G.N. Vayssilov, Y. Lykhach, A. Migani, T. Staudt, G.P. Petrova, N. Tsud, T. Skála, A. Bruix, F. Illas, K.C. Prince, V. Matolin, K.M. Neyman, J. Libuda, *Nat. Mater.* 10 (2011) 310–315.
- [30] N. Qiu, J. Zhang, Z. Wu, *Phys. Chem. Chem. Phys.* 16 (2014) 22659–22664.
- [31] M.I. Konsolakis, S.A.C. Carabineiro, E. Papista, G.E. Marnellos, P.B. Tavares, J. Agostinho Moreira, Y. Romaguera-Barcelay, J.L. Figueiredo, *Catal. Sci. Technol.* 5 (2015) 3714–3727.
- [32] C.-J. Pan, M.-C. Tsai, W.-N. Su, J. Rick, N.G. Akalework, A.K. Agegnehu, S.-Y. Cheng, B.-J. Hwang, *J. Taiwan Inst. Chem. Eng.* 74 (2017) 154–186.
- [33] M. Konsolakis, *Appl. Catal. B: Environ.* 198 (2016) 49–66.
- [34] L. Dong, X. Yao, Y. Chen, *Chin. J. Catal.* 34 (2013) 851–864.
- [35] G.G. Xanthopoulou, V.A. Novikov, Y.A. Knysh, A.P. Amosov, *Eurasian Chem. J.* 17 (2015) 17–32.
- [36] S.Y. Yao, W.Q. Xu, A.C. Johnston-Peck, F.Z. Zhao, Z.Y. Liu, S. Luo, S.D. Senanayake, A. Martínez-Arias, W.J. Liu, J.A. Rodriguez, *Phys. Chem. Chem. Phys.* 16 (2014) 17183–17195.
- [37] C.G. Maciel, T.D.F. Silva, M.I. Hirooka, M.N. Belgacem, J.M. Assaf, *Fuel* 97 (2012) 245–252.
- [38] W.-W. Wang, W.-Z. Yu, P.-P. Du, H. Xu, Z. Jin, R. Si, C. Ma, S. Shi, C.-J. Jia, C.-H. Yan, *ACS Catal.* 7 (2017) 1313–1329.
- [39] Y. Cui, W.-L. Dai, *Catal. Sci. Technol.* 6 (2016) 7752–7762.
- [40] D.G. Araiza, A. Gómez-Cortés, G. Díaz, *Catal. Today* 282 (2017) 185–194.
- [41] S. Saitzek, J.-F. Blach, S. Villain, J.-R. Gavarri, *Phys. Status Solidi* 205 (2008) 1534–1539.
- [42] P. Espen, H. Nullens, F. Adams, *Nucl. Instrum. Methods* 145 (1977) 579–582.
- [43] R. Barthos, A. Hegyessy, S. Klébert, J. Vallyon, *Microporous Mesoporous Mater.* 207 (2015) 1–8.
- [44] J. Xu, J. Harmer, G. Li, T. Chapman, P. Collier, S. Longworth, S.C. Tsang, *Chem. Commun. (Camb.)* 46 (2010) 1887–1889.
- [45] G. Tsilomelekis, S. Boghosian, *Catal. Sci. Technol.* 3 (2013) 1869–1888.
- [46] C. Andriopoulou, A. Trimpalis, K.C. Petalidou, A. Sgoura, A.M. Efstathiou, S. Boghosian, *J. Phys. Chem. C* 121 (2017) 7931–7943.
- [47] M. Farahmandjou, M. Zarinkamar, J. Ultrafine Grained Nanostruct. *Mater.* 48 (2015) 5–10.
- [48] M. Konsolakis, Z. Ioakimidis, T. Kraia, G. Marnellos, *Catal. Today* 6 (2016) 39.
- [49] P. Zhu, M. Liu, R. Zhou, *Indian J. Chem.* 51 (2012) 1529–1537.
- [50] J. Liu, Z. Zhao, J. Wang, C. Xu, A. Duan, G. Jiang, Q. Yang, *Appl. Catal. B: Environ.* 84 (2008) 185–195.
- [51] J.-Y. Luo, M. Meng, X. Li, X.-G. Li, Y.-Q. Zha, T.-D. Hu, Y.-N. Xie, J. Zhang, *J. Catal.* 254 (2008) 310–324.
- [52] S. Jampa, K. Wangkawe, S. Tantisriyanurak, J. Changpradit, A.M. Jamieson, T. Chaisuan, A. Luengnarumitchai, S. Wongkasemjit, *Int. J. Hydrogen Energy* 42 (2017) 5537–5548.
- [53] A. Aboukais, M. Skaf, S. Hany, R. Cousin, S. Aouad, M. Labaki, E. Abi-Aad, *Mater. Chem. Phys.* 177 (2016) 570–576.
- [54] P. Zhu, J. Li, Q. Huang, S. Yan, M. Liu, R. Zhou, *J. Nat. Gas Chem.* 18 (2009) 346–353.
- [55] X. Guo, R. Zhou, *Catal. Sci. Technol.* 6 (2016) 3862–3871.
- [56] R.S. Sundar, S. Deevi, *J. Nanopart. Res.* 8 (2006) 497–509.
- [57] N. Acerbi, S.C. Tsang, S. Golunski, P. Collier, *Chem. Commun.* (2008) 1578–1580.
- [58] C. Wang, Q. Cheng, X. Wang, K. Ma, X. Bai, S. Tan, Y. Tian, T. Ding, L. Zheng, J. Zhang, X. Li, *Appl. Surf. Sci.* 422 (2017) 932–943.
- [59] J. Wang, L. Zhong, J. Lu, R. Chen, Y. Lei, K. Chen, C. Han, S. He, G. Wan, Y. Luo, *Mol. Catal.* 443 (2017) 241–252.
- [60] M. Konsolakis, S.A.C. Carabineiro, G.E. Marnellos, M.F. Asad, O.S.G.P. Soares, M.F.R. Pereira, J.J.M. Órfão, J.L. Figueiredo, *J. Colloid Interface Sci.* 496 (2017) 141–149.
- [61] S.A.C. Carabineiro, S.S.T. Bastos, J.J.M. Órfão, M.F.R. Pereira, J.J. Delgado, J.L. Figueiredo, *Appl. Catal. A: Gen.* 381 (2010) 150–160.
- [62] S.A.C. Carabineiro, A.M.T. Silva, G. Dražić, P.B. Tavares, J.L. Figueiredo, *Catal. Today* 154 (2010) 21–30.
- [63] M. Konsolakis, S.A.C. Carabineiro, G.E. Marnellos, M.F. Asad, O.S.G.P. Soares, M.F.R. Pereira, J.J.M. Órfão, J.L. Figueiredo, *Inorg. Chim. Acta* 455 (2017) 473–482.
- [64] S.A.C. Carabineiro, M. Konsolakis, G.E.N. Marnellos, M.F. Asad, O.S.G.P. Soares, P.B. Tavares, M.F.R. Pereira, J.J. De Melo Órfão, J.L. Figueiredo, *Molecules* 21 (2016) 644.
- [65] M. Piumetti, T. Andana, S. Bensaid, N. Russo, D. Fino, R. Pirone, *Nanoscale Res. Lett.* 11 (2016) 165.
- [66] B. Solsona, R. Sanchis, A. Dejoz, T. García, L. Ruiz-Rodríguez, J. López Nieto, J. Cecilia, E. Rodríguez-Castellón, *Catal. Today* 7 (2017) 96.
- [67] F. Zhang, P. Wang, J. Koberstein, S. Khalid, S.W. Chan, *Surf. Sci.* 563 (2004) 74–82.
- [68] J. Giménez-Mañogil, A. Bueno-López, A. García-García, *Appl. Catal. B: Environ.* 152–153 (2014) 99–107.
- [69] J.P. Espinós, J. Morales, A. Barranco, A. Caballero, J.P. Holgado, A.R. González-Elipe, A.R. Gonza, *J. Phys. Chem. B* 106 (2002) 6921–6929.
- [70] M.C. Biesinger, L.W.M. Lau, A.R. Gerson, R.S.C. Smart, *Appl. Surf. Sci.* 257 (2010) 887–898.
- [71] M.C. Biesinger, B.R. Hart, R. Polack, B.A. Kobe, R.S.C. Smart, *Miner. Eng.* 20 (2007) 152–162.
- [72] L. Ilieva, P. Petrova, G. Pantaleo, R. Zanella, L.F. Liotta, V. Georgiev, S. Boghosian, Z. Kaszkur, J.W. Sobczak, W. Lisowski, A.M. Venezia, T. Tabakova, *Appl. Catal. B: Environ.* 188 (2016) 154–168.
- [73] E. Mamontov, T. Egami, R. Brezny, M. Koranne, S. Tyagi, *J. Phys. Chem. B* 104 (2000) 11110–11116.
- [74] J. Sun, L. Zhang, C. Ge, C. Tang, L. Dong, *Cuihua Xuebao/Chin. J. Catal.* 35 (2014) 1347–1358.
- [75] S. Yao, K. Mudiyansele, W. Xu, A.C. Johnston-Peck, J.C. Hanson, T. Wu, D. Stacchiola, J.A. Rodriguez, H. Zhao, K.A. Beyer, K.W. Chapman, P.J. Chupas, A. Martínez-Arias, R. Si, T.B. Bolin, W. Liu, S.D. Senanayake, *ACS Catal.* 4 (2014) 1650–1661.
- [76] L. Qi, Q. Yu, Y. Dai, C. Tang, L. Liu, H. Zhang, F. Gao, L. Dong, Y. Chen, *Appl. Catal. B: Environ.* 119–120 (2012) 308–320.
- [77] A.-P. Jia, S.-Y. Jiang, J.-Q. Lu, M.-F. Luo, *J. Phys. Chem. C* 114 (2010) 21605–21610.
- [78] H. Shang, X. Zhang, J. Xu, Y. Xan, *Front. Chem. Sci. Eng.* 11 (2017) 603–612, <http://dx.doi.org/10.1007/s11705-017-1661-z>.
- [79] Z. Hu, X. Liu, D. Meng, Y. Guo, Y. Guo, G. Lu, *ACS Catal.* 6 (2016) 2265–2279.
- [80] M. Piumetti, S. Bensaid, T. Andana, M. Dosa, C. Novara, F. Giorgis, N. Russo, D. Fino, *Catal. Today* 7 (2017) 174.